Dalton Transactions

ROYAL SOCIETY OF CHEMISTRY

PAPER

View Article Online
View Journal | View Issue

Cite this: *Dalton Trans.*, 2026, **55**, 4574

Crystal growth of metal tellurides from a boron–tellurium mixture: MTr_2Te_4 (M = Sr, Eu; Tr = In, Ga)

Subhendu Jana, E. A. Chirantha Edirisinghe, Machima Mongkhonratanachai and Paul A. Maggard *

A boron–tellurium mixture was employed as a reactive molten salt to prepare single crystals and polycrystalline powders of three ternary tellurides, MTr_2Te_4 (M = Sr, Eu; Tr = In, Ga), starting from binary metal oxides. This method represents a simple and efficient synthetic route wherein all reagents can be loaded in air. Single crystal X-ray diffraction was used to characterize the structures of β-$EuGa_2Te_4$ (**1**; space group: *Imma*), α-$EuIn_2Te_4$ (**2**; *Cccm*), and $SrGa_2Te_4$ (**3**; *I*4/*mcm*). Their structures are similarly comprised of the packing of $^1_\infty[Tr_2Te_4]^{2-}$ (Tr = Ga or In) chains separated and charge balanced by the divalent cations (M = Eu or Sr). Distinctive differences in the three structures stem from the arrangements of the divalent cation sites, with two different ordered arrangements found for the Eu cations in **1** and **2**, with the former representing a novel polymorph of $EuGa_2Te_4$. By contrast, the Sr cations in **3** adopt a fully disordered arrangement (50% occupancy) of the divalent cation sites. Results of total energy calculations show that the α-polymorphs of $EuGa_2Te_4$ and $EuIn_2Te_4$ are slightly lower in energy than the β-polymorphs. Optical bandgaps were measured using solid-state UV-Vis-NIR techniques, finding that all three exhibit semiconducting properties with direct transitions of 1.10(2) eV, 1.03(2) eV, and 0.93(2) eV, respectively. Electronic structure calculations show that their band gaps stem predominantly from filled Te p-orbitals and empty Ga/In s- and p-orbitals at the edges of their valence and conduction bands, respectively. Hence, a convenient and simple method for the preparation of metal tellurides is demonstrated, thereby unlocking the door to their much broader synthetic exploration.

Received 20th January 2026,
Accepted 23rd February 2026

DOI: 10.1039/d6dt00156d

rsc.li/dalton

I. Introduction

The structural chemistry of chalcogenides differs significantly from oxides due to the significant changes in metal-coordination environments and their polyhedra, which condense together to form a variety of new structures possessing from zero- to three-dimensional connectivity.[1–4] These diverse structures also give rise to a broad array of technological properties, such as useful for potential applications in thermoelectrics, superconductors, magnetic materials, or as nonlinear optical materials.[5–10] Accurate characterization of their crystalline structures and measurements of the physical properties of chalcogenides relies stringently upon their preparation as large single crystals and/or as phase-pure polycrystalline compounds.[11] However, traditional solid-state synthesis methods, such as sealed tube methods, nearly always result in the inadvertent introduction of oxide impurities. This occurs either through the partial surface oxidation of the starting reagents handled within a glovebox, *e.g.*, such as for easily-oxidized alkali- and alkaline-earth metals and rare-earth elements, and because of an imperfect vacuum when sealing the reagents inside fused-silica tubing.

Recently, the boron chalcogen mixture (BCM) method has emerged as an effective technique to synthesize metal sulfides and selenides starting from metal–oxide reagents. In this approach, elemental B is added as an efficacious oxygen scavenger that leads, *via* boron–chalcogenide intermediates, to the formation of thermodynamically-stable B_2O_3.[11–14] This side product can subsequently be removed by dissolution in ethanol. The *in situ* produced B_2O_3 remains molten above ~723 K and hypothetically can also act as a flux and can significantly accelerate the crystal growth of the metal-chalcogenide product. As most of the oxide starting materials used in the BCM method are neither moisture nor air-sensitive, they can conveniently be handled in ambient atmosphere. By contrast, the synthesis of metal chalcogenides *via* conventional solid-state methods typically requires a glovebox, as most of the elemental metals undergo rapid oxidation when exposed to ambient atmosphere. Given these advantages, a growing number of polycrystalline metal sulfides and selenides have been produced by the BCM method. These reactions are found to proceed *via* the formation of intermediate boron sulfide

Department of Chemistry and Biochemistry, Baylor University, Waco, Texas 76706, USA. E-mail: Paul_Maggard@baylor.edu

(*e.g.*, BS and B_2S_3) and boron selenide (*e.g.*, B_2Se_3) phases. The synthetic preparation of metal tellurides by this method, specifically by using a boron–tellurium mixture, has yet to be investigated to the best of our knowledge. Additionally, no boron–tellurides are currently known, with the exception of amorphous B_3Te_7.[11,15] Hence, it has been unclear whether elemental tellurium, with a lower electronegativity, would be as effective in combination with boron *via* this approach.

The present investigation explores the boron–tellurium mixture (BTM) in the initial test preparation of the EuTe binary, followed by the synthesis of three ternary metal-tellurides in the MTr_2Te_4 (M = Sr, Eu; Tr = In, Ga) family. Using the BTM method, single crystals of α-$EuIn_2Te_4$ (**2**), $SrGa_2Te_4$ (**3**), and the new β-$EuGa_2Te_4$ (**1**) were successfully grown and characterized through single crystal X-ray diffraction. Previous studies within this chemical family have reported the α-polymorph of $EuGa_2Te_4$, along with $SrGa_2Te_4$ and α-$EuIn_2Te_4$, which were only obtained as powders and structurally characterized using Rietveld methods.[16,17] The current research has unveiled more accurate structural models and three fascinating arrangements (50% occupation) of the divalent metal–cation sites. Two distinct ordered configurations of the Eu cations have been revealed in **1** and **2**, and a fully disordered configuration of the Sr cations is described for **3**. Also described herein are the first reported measurements of their optical properties and calculated electronic structures using density functional theory methods. Thus, these findings illustrate the successful application of the BTM method in the synthesis of metal-tellurides, providing a convenient and valuable synthetic pathway that will motivate broader synthetic explorations.

II. Experimental

II.A. Materials used

Single crystals and polycrystalline phases of β-$EuGa_2Te_4$ (**1**), α-$EuIn_2Te_4$ (**2**), and $SrGa_2Te_4$ (**3**) were synthesized using the BTM method from the following starting reagents: Eu_2O_3 powder (Alfa Aesar, 99.99% purity), SrO powder (Alfa Aesar, 99.5%), Ga pellets (Alfa Aesar, 99.999% purity), In powder (Alfa Aesar, 99.999% purity), Te pieces (Sigma Aldrich, 99.999% purity), and B powder (Beantown chemical, 99.9% purity). Since all the starting materials are air-stable, all the chemicals could be mixed and the reaction loaded in an ambient atmosphere. As SrO is air sensitive, it was stored in the glovebox prior to use.

II.B. Synthetic procedures

The preparation of EuTe starting from its oxide, Eu_2O_3, was first tested using the boron–tellurium mixture (BTM) method. In this reaction, a stoichiometric amount of Eu_2O_3 (84 mg, 0.239 mmol) was combined in air in stoichiometric quantities with Te pieces (60.9 mg, 0.477 mmol) and B powder (5.2 mg, 0.480 mmol). This mixture was then loaded into a heavily carbon-coated fused-silica tube with an 8 mm outer diameter (OD) in ambient atmosphere. The vessel was then sealed under vacuum using a natural gas torch, loaded into a muffle furnace, and heated to 1223 K over 16 h. After reacting at 1223 K for 30 h, the reaction was cooled to 823 K at a 20 K h^{-1} rate. The furnace was then switched off and allowed to radiatively cool to room temperature inside the furnace. The final products were washed with ethanol to remove the B_2O_3 side product. A few red plate-shaped crystals were selected for analysis by single crystal and powder X-ray diffraction techniques, confirming the formation of high purity EuTe (Fig. S1).

Single crystals of β-$EuGa_2Te_4$ (**1**) were next prepared starting from a stoichiometric mixture of Eu_2O_3 powder (42.1 mg, 0.120 mmol), Ga (33.3 mg, 0.478 mmol), Te (122 mg, 0.956 mmol), and B powder (2.6 mg, 0.240 mmol). All reactants were mixed and loaded within a heavily carbon-coated 8 mm OD fused-silica tube and sealed under vacuum. A parallel procedure was conducted for preparing reactions which yielded α-$EuIn_2Te_4$ (**2**) and $SrGa_2Te_4$ (**3**). For **2**, the reactant mixture incorporated 38 mg (0.108 mmol) of Eu_2O_3 powder, 49.6 mg (0.432 mmol) of In powder, 110.1 mg (0.863 mmol) of Te pieces, and 2.3 mg (0.213 mmol) of B powder. While for **3**, the reaction mixture contained SrO (34.1 mg, 0.329 mmol), Ga pieces (45.8 mg, 0.657 mmol), Te powder (167.7 mg, 1.314 mmol), and B powder (2.4 mg, 0.222 mmol). During the reaction, all three fused-silica vessels were heated to 1223 K at a rate of 72 K h^{-1}, held for 48 h, and then cooled to 823 K at a rate of 12 K h^{-1} in a muffle furnace. Finally, the furnace was turned off and allowed to reach room temperature by radiative cooling inside the furnace. The tubes were opened, and the products were washed using ethanol inside a fume hood. **Caution:** *Telluride compounds can potentially react in the presence of moisture and produce toxic H_2Te gas. So, all reactions should be handled in a fume hood following safety protocols*. The products were air-dried and analyzed under an optical microscope, revealing black, block-shaped crystals for each. Chemical compositions for each were evaluated using energy dispersive spectroscopy on their respective crystals, as given in the SI (shown in Fig. S2–S4). Synthesis of 0.5 g amounts of each used 12 mm OD fused-silica tubing, following the same heating profiles. Phase purities were analyzed using powder X-ray diffraction data, given in the SI (shown in Fig. S5).

II.C. Characterization by X-ray diffraction (XRD)

The structures of **1**, **2**, and **3** were determined at room-temperature using single crystal X-ray diffraction on a Bruker D8 Quest diffractometer equipped with a Photon III mixed mode detector. The respective crystals were mounted on a goniometer separately under Paratone-N oil, and the XRD datasets were collected using a Mo Kα (λ = 0.71073 Å) radiation source. The APEX4 software[18] automatically determined the data collection strategy and processed the data. The quality of each of the crystals was initially evaluated from the diffraction peak shapes and unit cells, as obtained from a fast scan data of 180 frames using a 2 seconds per frame exposure time, a 50 mm crystal-to-detector distance, and a frame width of 1°. Full single crystal data sets were then measured at an exposure time of 7 seconds per frame, a crystal-to-detector distance of

50 mm, and a frame width of 0.5°. Absorption corrections were performed using the multi-scan method of the SADABS software package.[19] Based on extinction conditions, the XPREP software[20] suggested a body-centered *Imma* space group and base-centered *Cccm* space group for **1** and **2**, respectively. Both crystal structures were solved using the SHELXT program.[21] The initial solution of **1** gave eight crystallographically-independent atomic sites, assigned to one Eu, three Ga, and four Te sites based on their respective peak heights and coordination environments. Full structural refinements were carried out using the least squares method as implemented in the SHELXL program.[22] Similarly, the structure of **2** was solved and refined except that a twin law of [−1 0 0 0 0 1 0 1 0] needed to be applied with a refined BASF value of ∼0.197. Lastly, the structure of **3** was solved and refined in the *I*4/*mcm* space group. The final model gave three crystallographically-independent atomic sites, one 50%-occupied Sr site, and a single site for both Ga and Te. The PLATON software package[23] was used to standardize the atomic positions and to check for any missing symmetry elements. The structural refinement details are summarized in Table 1, with full listings of atomic coordinates, anisotropic thermal parameters, and selected interatomic distances given in the SI (Tables S4–S10).

Phase purities of the bulk polycrystalline powders were confirmed by powder X-ray diffraction (PXRD) measurements at room temperature. The PXRD data were collected over a 2θ range of 10°–70° using a Cu Kα source on a Bruker D2 Phaser instrument with a step size of 0.015°.

II.D. Optical bandgap measurements

The optical absorption data of polycrystalline MTr_2Te_4 powders were recorded using a JASCO V-770 UV-Vis-NIR spectroscopy over a wavelength range of 2500 nm (0.50 eV) to 200 nm (6.2 eV) to evaluate the bandgaps of the polycrystalline samples. Tauc plots were used to estimate the direct and indirect band transition energies of the polycrystalline products, using methods described previously.[24]

II.E. Electronic structure calculations

Density functional theory (DFT) calculations of the electronic structures of **1**, **2**, and **3** were conducted using the Projector Augmented Wave (PAW) method within the *Vienna Ab initio simulation package* (VASP; ver. 6.3.2).[25,26] The generalized gradient approximation method was used to treat the exchange–correlation functionals within the Perdew–Burke–Ernzerhof parametrization.[27] A plane-wave basis set with an energy cut-off threshold of 300 eV was used, consistent with the respective PAW pseudopotentials for each compound. These included the valence orbital sets for Eu (5s,5p,6s,4f,5d), Sr (4s,4p,5s), In (5s,5p), Ga (4s,4p), and Te (5s,5p). The criterion for reaching electronic self-consistency was fixed to less than 10^{-8} eV. For **1** and **2**, the strong on-site Coulomb interactions for the 4f orbitals of Eu were approximated at 7 eV, consistent with prior reports.[28] Spin–orbit coupling (SOC) was incorporated self-consistently in all calculations using non-collinear magnetic settings within VASP to correctly capture the effects of SOC. The structures were fully geometry relaxed until the norms on the atomic forces converged to less than 0.01 eV $Å^{-1}$. Density-of-states (DOS) calculations used *k*-point meshes of 4 × 2 × 6 (48 *k*-points), 6 × 4 × 4 (96 *k*-points), and 3 × 3 × 4 (50 *k*-points) for **1**, **2**, and **3**, respectively. For band structure calculations, the *k*-point paths within the Brillouin zones of the respective crystal structures were generated using SeeK-path[29] (Γ–Y–C0|Σ0–Γ–Z–A0|E0–T–Y|Γ–S–R–Z–T for **1**; Γ–X–F0|Σ0–Γ–Λ0|G0–X|Γ–R–W–S–Γ–T–W for **2**; Γ–X–M–Γ–Z–R–A–Z|X–R|M–A for **3**). Each reciprocal lattice direction in *k*-space was sampled at 10 intersecting *k*-points. Plots of the calculated DOS and band structures were generated using the SUMO package.[30]

Table 1 Crystallographic refinement details for the structures of **1**, **2**, and **3**

Compound	β-$EuGa_2Te_4$ (**1**)	α-$EuIn_2Te_4$ (**2**)	$SrGa_2Te_4$ (**3**)
Space group	*Imma*	*Cccm*	*I*4/*mcm*
a (Å)	11.5596(5)	7.1392(5)	8.2190(5)
b (Å)	23.0747(9)	11.6314(8)	
c (Å)	6.7187(3)	11.6903(9)	6.7270(5)
V ($Å^3$)	1792.11(13)	970.75(12)	454.42(6)
Z	8	4	2
ρ (g cm^{-3})	5.943	6.103	5.390
μ (mm^{-1})	25.55	22.79	24.22
$R(F)^a$	0.021	0.025	0.023
R_w $(F_o^2)^b$	0.064	0.056	0.049
S	1.08	1.14	1.00
δF (e $Å^{-3}$)	3.34/−0.86	1.82/−1.93	0.88/−1.36
No. of reflections	11 320	6769	1098
No. of independent reflections	1169	784	235

^{a} $R(F) = \sum||F_o| - |F_c||/\sum|F_o|$ for $F_o^2 > 2\sigma(F_o^2)$. ^{b} $R_w(F_o^2) = \{\sum[w(F_o^2 - F_c^2)^2]/\sum wF_o^4\}^{1/2}$. For $F_o^2 < 0$, $w = 1/[\sigma^2(F_o^2) + (mP)^2 + nP]$, where $P = (F_o^2 + 2F_c^2)/3$. Here *m* and *n* are 0.0351 and 1.2444, 0.0184 and 0, and 0.0251 and 7.4074 for **1**, **2**, and **3**, respectively.

III. Results and discussion

III.A. Boron–tellurium mixture (BTM) synthetic method

The approach of utilizing a BTM mixture to prepare metal tellurides was initially tested for feasibility starting from the inexpensive and air-stable europium(III) oxide, Eu_2O_3. The analogous boron–chalcogenide method for selenium and sulfur proceeds with the initial formation of boron chalcogenide intermediates. Subsequently, the volatile boron chalcogenides react and displace the oxygen atoms of the metal oxide, forming the B_2O_3 side product and the respective metal chalcogenides. The equivalent chemical reaction for the BTM method using tellurium is given by the balanced reactions shown below for the formation of EuTe (A) and $EuGa_2Te_4$ (B):

$$Eu_2O_3 + 2B + 2Te \rightarrow 2EuTe + B_2O_3 \quad (A)$$

$$Eu_2O_3 + 2B + 8Te + 4Ga \rightarrow 2EuGa_2Te_4 + B_2O_3 \quad (B)$$

The product of reaction (A) was obtained after heating at a temperature of 1223 K, followed by washing, yielding the high-

purity synthesis of EuTe as shown in Fig. S1 in the SI. It should be noted that Eu(III) is reduced to Eu(II) during the reaction, while B_2O_3 subsequently serves as a flux to facilitate crystal growth. Hence, relatively large, red-colored crystals of EuTe were found to grow throughout the mixture. Following the successful preparation of EuTe, the crystal growth of ternary metal-tellurides was next attempted in the MTr_2Te_4 (M = Sr, Eu; Tr = In, Ga) chemical systems, as represented in Scheme 1. By this same route, block-shaped single crystals of β-$EuGa_2Te_4$ (**1**), α-$EuIn_2Te_4$ (**2**), and $SrGa_2Te_4$ (**3**) could be obtained *via* reactions at 1223 K, as given in Scheme 1 and in reaction (B) for **1**. After washing, the products were observed to be stable in air for up to 2 months. Results of energy-dispersive spectroscopy, Fig. S2–S4 in the SI, confirmed homogeneous distributions of M (Eu and Sr), Tr (Ga and In), and Te in the approximate molar ratios of 1 : 2 : 4. While powder XRD data for the bulk powders of **1** indicated the formation of **1** along with minute secondary phases of Ga_2Te_3 (~5%) and unknown phase(s) (~2%) (Fig. S5(a)), the powder XRD data for **2** and **3** (Fig. S5(b and c)) showed evidence for the presence of a minute amount of ~2% elementary Te in the former and ~5% each of Ga_2Te_5 and Ga_2Te_3 in the latter. Hence, both binary and ternary metal tellurides could be efficiently obtained by this method that eliminates the need for air-sensitive starting reagents, such as elemental strontium or europium or their respective metal chalcogenides.

III.B. Structural characterization

The black, block-shaped crystals of **1**, **2**, and **3** were characterized by single-crystal XRD measurements to form in three different space groups, *Imma*, *Cccm*, and *I*4/*mcm*, respectively, and structure types. All three structures, illustrated in Fig. 1, are similarly comprised of linear chains of $^1_\infty[Tr_2Te_4]^{2-}$, (Tr = Ga or In) separated by divalent M cations (M = Eu or Sr). The structure of **1**, β-$EuGa_2Te_4$ shown in Fig. 1(a), has the largest unit cell (body-centered) of the three and crystallizes with two different $^1_\infty[Ga_2Te_4]^{2-}$ chains separated by the charge-balancing Eu cations. The two chains, shown in Fig. 2(a and b), are comprised of three crystallographically-independent Ga sites, each coordinated within distorted, $GaTe_4$ tetrahedra. These $GaTe_4$ tetrahedra condense *via* shared edges to form chains of $^1_\infty[Ga_2Te_4]^{2-}$ aligned down the *c*-axis, with the tetrahedra centered by Ga1 in the first chain and alternating Ga2/Ga3 in the second chain. By comparison, the analogous Ga-containing structure of **3**, *i.e.*, $SrGa_2Te_4$, exhibits a much smaller unit cell (~25% by volume) and a single symmetry-unique Ga-site within a similar $^1_\infty[Ga_2Te_4]^{2-}$ chain, Fig. 2d. All Ga–Te interatomic distances in both **1** and **3** occur within a narrow range of 2.631 Å to 2.637 Å. These distances are consistent with those in the previously reported β-$BaGa_2Te_4$ (2.609(1)–2.646(1) Å)[31] and α-$BaGa_2Te_4$ (2.622(1) Å) compounds.[32]

In the crystal structure of **2**, α-$EuIn_2Te_4$, each In atom is bonded to four Te atoms to form $^1_\infty[In_2Te_4]^{2-}$ chains of edge-shared $InTe_4$ tetrahedra, as described above for **1** and **3** and shown in Fig. 2(c). The unit cell volume of **2** is smaller than **1** (~50% by volume) and consists of a single symmetry-unique In atom and edge-shared chains. The trend in their cell volumes of **3** < **2** < **1** largely represents the growing number of MTr_2Te_4 formula units per unit cell, as illustrated in Fig. 1. Within the linear chains, the In–Te distances of $InTe_4$ tetrahedra occur within a range of 2.768 Å to 2.844 Å, which are about 6% to 8% larger than the Ga–Te distances. These In–Te interatomic distances are similar to those described in prior reports of $CsCdInTe_3$ (2.7602(3)–2.7862(7) Å),[33] $BaIn_2Te_4$ (2.7692(7)–2.8381(7) Å),[4] $CuInTe_2$ (2.7878(3) Å),[34] and $Ba_3Ag_3InTe_6$ (2.7625(7)–2.8257(5) Å).[35] The previously reported structure of α-$EuIn_2Te_4$ consisted of only its unit cell parameters and space group.[17] Notably, the reported unit cell volume is significantly smaller by ~49 $Å^3$ (about 5% to 6%), *i.e.*, 921.32 $Å^3$ *versus* 970.75(12) $Å^3$ in **2**. Hence, the capability to grow high-quality single crystals of **2** by the BTM method has dramatically increased the accuracy of its structure determination. Additionally, a Ga-containing version of this structure, $EuGa_2Te_4$, is reported to crystallize in this structure type, now

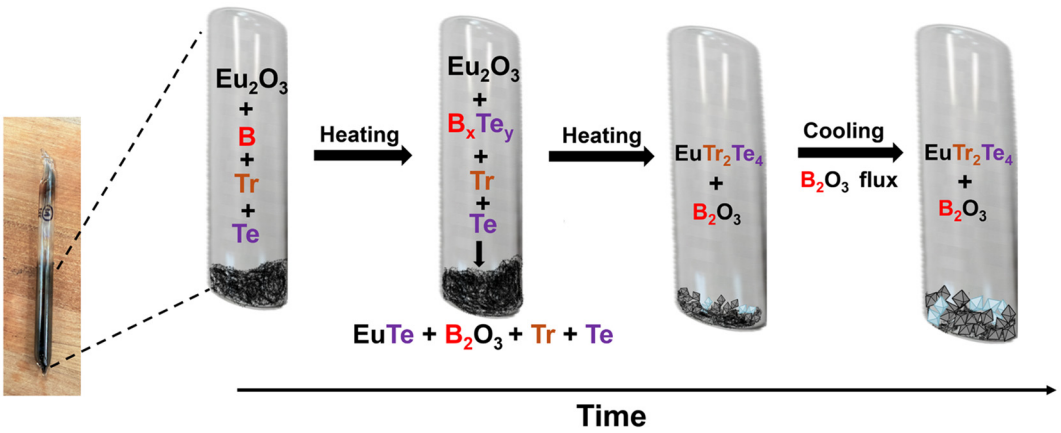

Scheme 1 Reaction scheme for the formation of $EuTr_2Te_4$ (Tr = In and Ga) using the BTM method. The proposed process involves the initial formation intermediate B_xTe_y phases, which then react with Eu_2O_3 to form the binary and/or ternary Eu-containing tellurides. The B_2O_3 side product possibly serves as a flux for enhancing crystal growth of the products. The formation of $SrGa_2Te_4$ is also proposed to follow an analogous pathway.

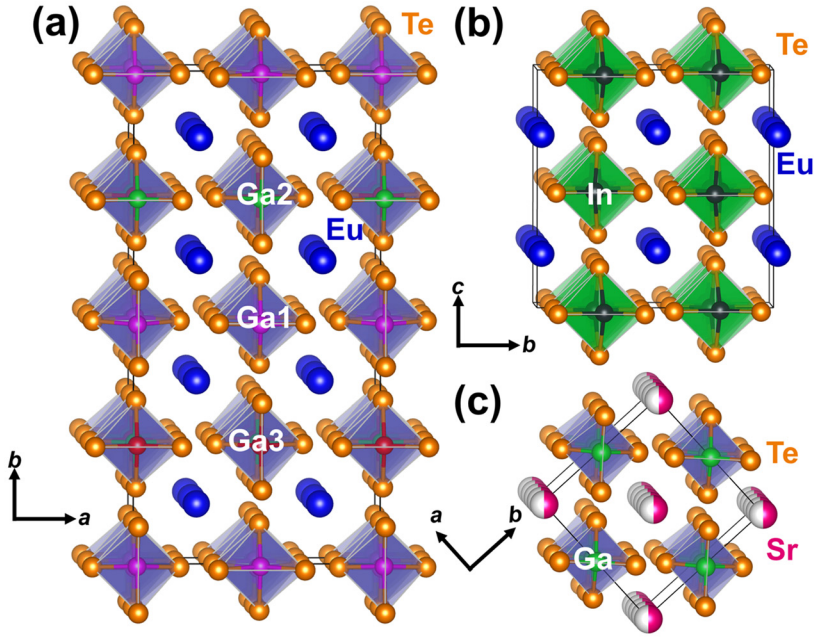

Fig. 1 Unit cell polyhedral views of the (a) β-$EuGa_2Te_4$, (b) α-$EuIn_2Te_4$, and (c) $SrGa_2Te_4$ structures viewed down the $^1_\infty[Tr_2Te_4]^{2-}$ chain directions of each.

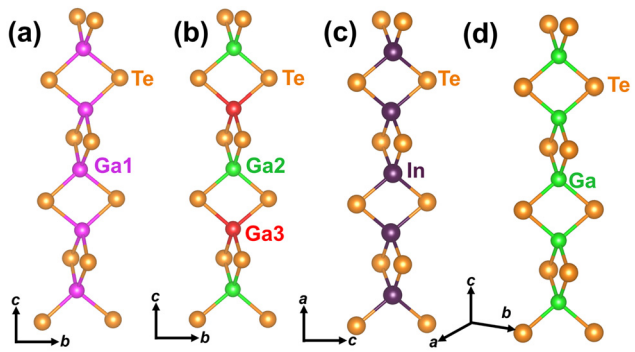

Fig. 2 View of the (a) $^1_\infty[Ga1_2Te_4]^{2-}$ and (b) $^1_\infty[Ga2Ga3Te_4]^{2-}$ chains in the β-$EuGa_2Te_4$ crystal structure. View of the (c) $^1_\infty[In_2Te_4]^{2-}$ and (d) $^1_\infty[Ga_2Te_4]^{2-}$ chains in the α-$EuIn_2Te_4$ and $SrGa_2Te_4$ crystal structures, respectively.

labeled as α-$EuGa_2Te_4$ to differentiate it from the new polymorph of β-$EuGa_2Te_4$ described above for **1**. In sum, these results show that $EuGa_2Te_4$ can crystallize in either of two structural arrangements shown in Fig. 1(c), with the α-polymorph reported previously and the β-polymorph discovered using the new BTM method.

The three different MTr_2Te_4 structure types in this family are distinguished by the different ordered and disordered configurations of the divalent cations (M = Sr, Eu) between the $^1_\infty[Tr_2Te_4]^{2-}$, (Tr = Ga or In) linear chains. Within each structure, the Sr and Eu cations occupy 50% of the available cation sites that reside between the chains of edge-shared $TrTe_4$ tetrahedra. This 50% occupancy of the M-site occurs in an ordered configuration for the Eu cations in **1** and **2**, but in a disordered arrangement for the Sr cations in **3**. In all three structures, the divalent cations are similarly coordinated by eight telluride anions, forming distorted, square antiprisms, as illustrated in Fig. 3 and Fig. S6 in the SI. The Eu–Te distances of $EuTe_8$ polyhedra occur in the range of 3.41 Å to 3.50 Å, consistent with prior reports for $EuCu_{0.66}Te_2$ (3.326(3)–3.481(4) Å) and Eu_2InTe_5 (3.3381(4)–3.5328(4) Å).[36,37] However, the two different ordered arrangements of $EuTe_8$ polyhedra in **1** and **2** are condensed *via* edge-sharing into double chains and single chains, respectively, illustrated in Fig. 3 (right). While both structures appear remarkably similar, the double edge-shared chains in **1** result in the occupation of a Ga2 site that tightly fits within the center of four $EuTe_8$ polyhedra. Its network of edge-shared $EuTe_8$ and $GaTe_4$ chains is relatively more condensed, with a larger number of shorter cation-cation distances, as compared to the structure of **2**. Given the relatively larger size of the In cations, and hence longer In–Te distances, the Eu cations in the structure of **2** form only single chains with the $InTe_4$ tetrahedra edge-sharing to only four neighboring $EuTe_8$ polyhedra. Though, it is notable that $EuGa_2Te_4$ is also reported to form with this structure type. The Sr cations in the structure of **3**, $SrGa_2Te_4$, do not exhibit an ordered configuration, but occupy 50% of the divalent cation sites in a fully random arrangement. The site-averaged Sr–Te distance of the $SrTe_8$ square antiprisms of **3** is 3.4715(2) Å, which is comparable to that found in previously reported compounds such as $SrScCuTe_3$ (3.3209(7)–3.7231(7) Å).[3] Given the almost-negligible larger size of the Sr cation as compared to the Eu cation, this has remarkably resulted in no discernible structural pre-

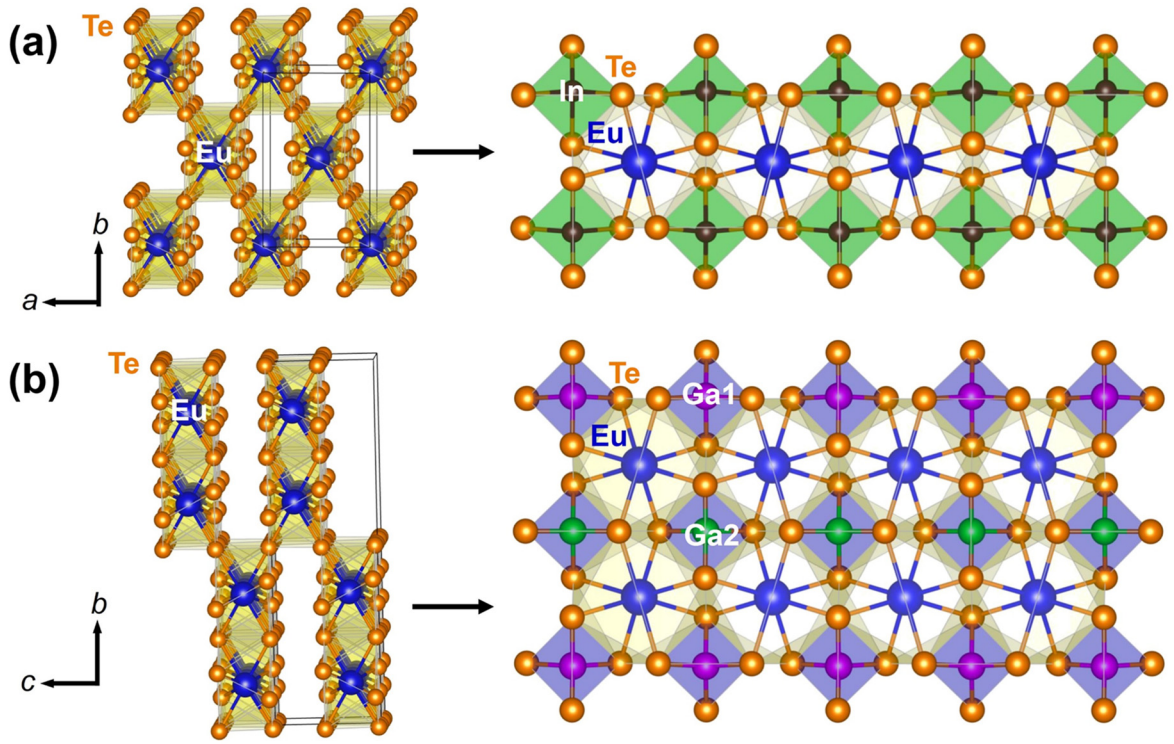

Fig. 3 Polyhedral views of the extended connectivity of $EuTe_8$ square antiprisms that form single edge-shared chains in α-$EuIn_2Te_4$ ((a), **2**) and double edge-shared chains in β-$EuGa_2Te_4$ ((b), **1**). The $TrTe_4$ (Tr = Ga or In) tetrahedra are omitted for clarity on the left and shown on the right to illustrate their overall connectivity with the Eu-based chains in each structure.

ferences such as represented by the ordered configurations of **1** or **2**.

III.C. Optical bandgaps and electronic structures

Metal chalcogenides have drawn interest for their optoelectronic properties, such as for nonlinear optical properties or solar energy conversion.[38] To elucidate their future compatibility for various potential optoelectronic applications, the optical properties of polycrystalline powders of β-$EuGa_2Te_4$ (**1**), α-$EuIn_2Te_4$ (**2**), and SrG_2Te_4 (**3**) were measured using UV-Vis diffuse reflectance techniques at room temperature. Tauc plots of polycrystalline samples showed evidence for direct band-to-band transitions at 1.10(2) eV, 1.03(2) eV, and 0.93(2) eV, respectively, as illustrated in Fig. S8 in the SI. These absorption-edge values are consistent with the black colors of all three compounds. However, distinct absorption edges indicative of lower-energy indirect transitions were either negative or potentially occur at energies lower than the detector limit of the instrument of ~0.5 to 0.7 eV and could not be excluded.

Density functional theory (DFT) calculations were employed to elucidate the electronic structures of **1**, **2**, and **3**. The resulting density-of-states (DOS) of the ordered, Eu-containing structures of **1** and **2** are plotted in Fig. 4(a and b), while the DOS for **3** is given in the SI (Fig. S10). As shown in Fig. 4, the total DOS (black line) of the MTr_2Te_4 structures are comprised of the atomic contributions from Te 5s/5p orbitals in both, and Ga 4s/p orbitals in **1** and In 5s/5p orbitals in **2**. The Te contributions predominate at the edge of the valence band (VB) in each, whereas the atomic contributions from the localized, filled Eu (4f) occur at deeper energies by about 1.5 eV. The conduction band (CB) edges consist of the empty 4s/p- and 5s/p-orbitals, respectively for Ga and In, which are strongly mixed with the Te 5p-orbitals. The calculated DOS for $SrGa_2Te_4$ is similarly constructed, as shown in Fig. S10 in the SI, minus any contributions from 4f-obitals. In all cases, the bandgaps from the DOS and band structure plots were calculated to be <0.5 eV. This is consistent with the underestimation of the calculated bandgaps of semiconductors *via* density functional theory methods, which is a well-documented issue.[39]

Total energy calculations were utilized to probe the relative energetic stabilities of the α- and β-polymorphs for both $EuGa_2Te_4$ and $EuIn_2Te_4$. The refined structures of **1** and **2** were used as the starting models for β-$EuGa_2Te_4$ and α-$EuIn_2Te_4$, while the previously reported structure for α-$EuGa_2Te_4$ was used.[17] The structure of the hypothetical β-$EuIn_2Te_4$ was modeled by replacing Ga with In in **1**. After full geometry relaxation of all four structures, the total energies were obtained and listed in Table 2. The β-polymorph of $EuGa_2Te_4$, as found herein using the BTM method, is found to be ~11 meV per formula higher in energy than its previously reported α-polymorph. The energetic difference is negligible and agrees with the synthetic preparation of both polymorphs with a change in reaction conditions, such as with temperature or using the BTM method. For $EuIn_2Te_4$, by contrast, the

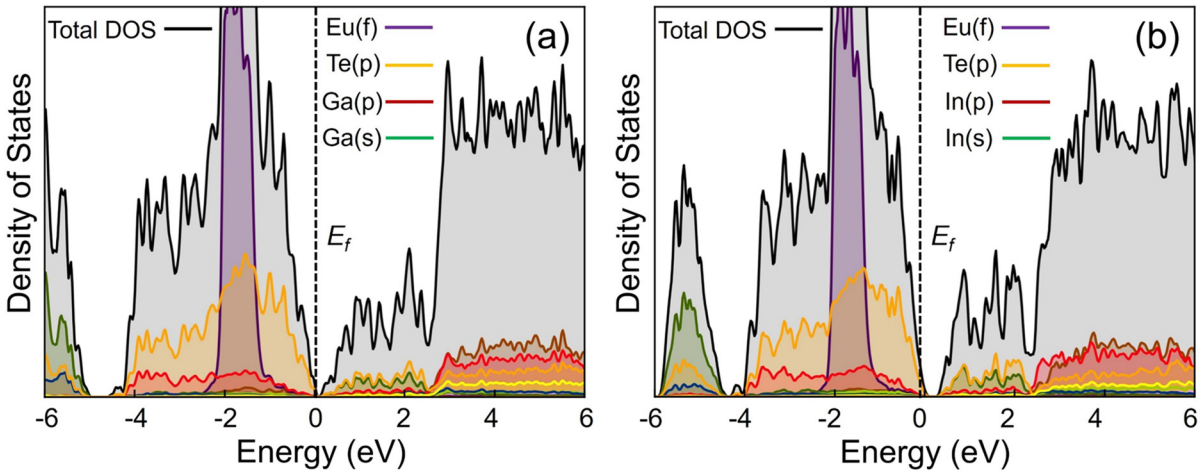

Fig. 4 Calculated density-of-states (DOS) plots for (a) β-$EuGa_2Te_4$ and (b) α-$EuIn_2Te_4$. The Fermi energy level is shown by a black dotted line at 0 eV. Individual atomic orbital contributions to the DOS are shown as colored lines.

Table 2 Calculated total energies of $EuGa_2Te_4$ and $EuIn_2Te_4$ within the two structure types of **1** and **2**, *i.e.*, as labeled as the α- and β-polymorphs for each

Composition	Polymorph	Total energy (eV per formula)	Source
$EuGa_2Te_4$	α-Type	−33.4064	Ref. 17
$EuGa_2Te_4$	β-Type (**1**)	−33.3955	This work
$EuIn_2Te_4$	α-Type (**2**)	−32.5644	This work
$EuIn_2Te_4$	β-Type	−32.5398	Unknown[a]

[a] This hypothetical polymorph was simulated from the structure of **1** by replacing Ga with In and performing a full geometry relaxation.

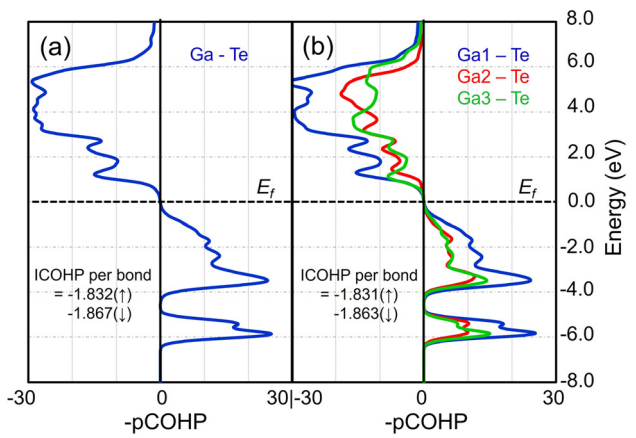

Fig. 5 The calculated Crystal Orbital Hamilton Populations (COHP) for the pairwise Ga–Te interactions in α-$EuGa_2Te_4$ (a) and β-$EuGa_2Te_4$ (**1**; (b)), with the Fermi levels (E_f) given as dashed lines at 0 eV. Positive and negative values indicate bonding and antibonding interactions, respectively.

α-polymorph is lower in energy by ~25 meV per formula. This agrees with the experimental results, which demonstrate the crystallization of α-$EuIn_2Te_4$ rather than the alternate β-polymorph. Hence, the β-polymorph occurs at a higher energy than the α-polymorph in both cases, but with the difference being larger for the In-based compound.

Analysis of changes in the covalent bonding character within the two different polymorphs for $EuGa_2Te_4$ and $EuIn_2Te_4$ was examined using Crystal Orbital Hamilton Populations (COHP) within the LOBSTER package.[40,41] The bonding and antibonding character for the two-center interactions between Tr–Te (Tr = Ga and In) are plotted *versus* energy in Fig. 5 and in Fig. S12 in the SI, respectively. For α-$EuGa_2Te_4$ in Fig. 5a, the Ga–Te interactions for the single symmetry-unique Ga show a clear transition from strongly bonding to strongly antibonding with increasing energy, passing through a nonbonding region near the Fermi level. Similarly, the three symmetry-unique Ga atoms in α-$EuGa_2Te_4$, *i.e.*, Ga1, Ga2, and Ga3 separately plotted in Fig. 5b, all exhibit the same pattern. The integrated COHP, or ICOHP, is a measure of the shared electrons and the strength of covalent bonding. The ICOHPs' for Ga–Te are surprisingly similar, with an average of 1.83 and 1.86 electrons per bond for the respective up/down spin populations of both polymorphs. The same general trend holds for the In–Te interactions for both polymorphs of $EuIn_2Te_4$, with average ICOHP's of 1.62 and 1.65 electrons for the respective up/down spin populations in each case. The latter ICOHPs are reflective of a weaker covalent character. Changes in the ionic bonding and electrostatic forces between the energetically similar polymorphs were next analyzed. The Madelung energies for the β-polymorphs of each structure were found to be only slightly larger, as calculated in LOBSTER from the Löwdin atomic charges. The β-polymorphs of $EuGa_2Te_4$ and $EuIn_2Te_4$ yielded Madelung energies of −0.286 and −0.271 eV per formula, respectively, as compared to the Madelung energies for the α-polymorphs of −0.280 and −0.270 eV per formula, respectively. Hence, the different ordering patterns of the Eu cations have a relatively negligible effect

on either the covalent or ionic bonding, consistent with their very similar total energies listed in Table 2. Future research is warranted to assess how finer-level differences in vibrational entropies may determine the energetic preferences of polymorph formation as a function of temperature.

IV. Conclusions

Three ternary metal-tellurides in the MTr_2Te_4 family, *i.e.*, β-$EuGa_2Te_4$ (**1**), α-$EuIn_2Te_4$ (**2**), and $SrGa_2Te_4$ (**3**) were synthesized using a new boron–tellurium mixture method and characterized by single crystal and powder XRD techniques. This method overcomes the challenges typically associated with metal-telluride synthesis *via* the use of metal oxide and air-stable reagents. All three structures were found to be similar and comprised of edge-shared chains of $TrTe_4$ tetrahedra (Tr = Ga or In) aligned and separated by the charge-balancing divalent cations (M = Sr or Eu). The structures principally differ in the arrangement of the divalent cations in the interchain atomic sites, which are 50% occupied for all three structures. The structures of **1** and **2** represent two ordered configurations of the Eu cations, yielding edge-shared $EuTe_8$ square antiprisms condensed into double chains in **1** and single chains in **2**. Conversely, the Sr cations adopt a fully disordered occupancy of the divalent cation sites in **3**. All three show small, direct band transitions between about 0.9 and 1.10 eV, consistent with a semiconducting nature and the black colors of their crystals. Electronic structure calculations on the two possible polymorphs of $EuGa_2Te_4$ and $EuIn_2Te_4$ reveal that the α polymorph is only slightly lower in energy than the β-polymorph. Hence, a convenient and simple synthetic pathway for the preparation of metal-tellurides is demonstrated, also yielding the formation of the new β-$EuGa_2Te_4$ polymorph.

Author contributions

Formal analysis, investigation, visualization, and writing: SJ, EACE, MM, and PM; project administration and supervision: PM.

Conflicts of interest

There are no conflicts to declare.

Data availability

Supplementary information (SI): characterization data include the EDX spectra, elemental maps, and additional results of electronic structure calculations. See DOI: https://doi.org/10.1039/d6dt00156d.

CCDC 2415584 (β-$EuGa_2Te_4$), 2415585 (α-$EuIn_2Te_4$) and 2486668 ($SrGa_2Te_4$) contain the supplementary crystallographic data for this paper.[42a–c]

Acknowledgements

Primary support of these research efforts is acknowledged by the Department of Chemistry and Biochemistry at Baylor University. This work utilized the High-Performance Research Computing FASTER cluster at Texas A&M University through allocation CHE240107 from the Advanced Cyberinfrastructure Coordination Ecosystem: Services & Support (ACCESS) program 38 which is supported by U.S. National Science Foundation grants #2138259, #2138286, #2138307, #2137603, and #2138296.

References

1 M. A. Viti, Z. Li, C. Wolverton and M. G. Kanatzidis, Dimensional Reduction Guides Electronic Structure Evolution in the $A_nCu_{4-n}SnS_4$ Semiconductor Series, *J. Am. Chem. Soc.*, 2025, **147**, 29994–30008.
2 S. O'Donnell, I. A. Leahy, S. Jana, E. A. Gabilondo, P. S. Halasyamani, P. A. Maggard and R. W. Smaha, Magnetic Properties and Large Second-Harmonic Generation Response of a Chiral Ternary Chalcogenide: Eu_2SiSe_4, *Chem. Mater.*, 2025, **37**, 5036–5042.
3 M. Ishtiyak, S. Jana, R. Karthikeyan, M. Ramesh, B. Tripathy, S. K. Malladi, M. K. Niranjan and J. Prakash, Syntheses of Five New Layered Quaternary Chalcogenides $SrScCuSe_3$, $SrScCuTe_3$, $BaScCuSe_3$, $BaScCuTe_3$, and $BaScAgTe_3$: Crystal Structures, Thermoelectric Properties, and Electronic Structures, *Inorg. Chem. Front.*, 2021, **8**, 4086–4101.
4 M. Ishtiyak, S. Jana, S. Narayanswamy, A. K. Nishad, G. Panigrahi, P. P. Bhattacharjee and J. Prakash, Intrinsic Extremely Low Thermal Conductivity in $BaIn_2Te_4$: Synthesis, Crystal Structure, Raman Spectroscopy, Optical, and Thermoelectric Properties, *J. Alloys Compd.*, 2019, **802**, 385–393.
5 C. Zhou, Y. K. Lee, Y. Yu, S. Byun, Z.-Z. Luo, H. Lee, H. Ge, Y.-L. Lee, X. Chen, J. Y. Lee, O. Cojocaru-Mirédin, H. Chang, J. Im, S.-P. Cho, M. Wuttig, V. P. Dravid, M. G. Kanatzidis and I. Chung, Polycrystalline SnSe with a Thermoelectric Figure of Merit Greater than the Single Crystal, *Nat. Mater.*, 2021, **20**, 1378–1384.
6 S. Margadonna, Y. Takabayashi, M. T. McDonald, K. Kasperkiewicz, Y. Mizuguchi, Y. Takano, A. N. Fitch, E. Suard and K. Prassides, Crystal Structure of the New $FeSe_{1-x}$ Superconductor, *Chem. Commun.*, 2008, **43**, 5607–5609.
7 A. P. Ramirez, R. J. Cava and J. Krajewski, Colossal Magnetoresistance in Cr-Based Chalcogenide Spinels, *Nature*, 1997, **386**, 156–159.

8 S. Jana, S. O'Donnell, I. A. Leahy, A. Koldemir, R. Pöttgen, R. W. Smaha and P. A. Maggard, Synthesis, Crystal Structure, and Physical Properties of the Eu(II)-Based Selenide Semiconductor: $EuHfSe_3$, *J. Mater. Chem. C*, 2024, **12**, 11769–11777.
9 A. Wustrow, B. Key, P. J. Phillips, N. Sa, A. S. Lipton, R. F. Klie, J. T. Vaughey and K. R. Poeppelmeier, Synthesis and Characterization of $MgCr_2S_4$ Thiospinel as a Potential Magnesium Cathode, *Inorg. Chem.*, 2018, **57**, 8634–8638.
10 P. G. Schunemann, K. L. Schepler and P. A. Budni, Nonlinear Frequency Conversion Performance of $AgGaSe_2$, $ZnGeP_2$, and $CdGeAs_2$, *MRS Bull.*, 1998, **23**, 45–49.
11 L. S. Breton, V. V. Klepov and H.-C. zur Loye, Facile Oxide to Chalcogenide Conversion for Actinides Using the Boron–Chalcogen Mixture Method, *J. Am. Chem. Soc.*, 2020, **142**, 14365–14373.
12 L.-M. Wu and D.-K. Seo, New Solid−Gas Metathetical Synthesis of Binary Metal Polysulfides and Sulfides at Intermediate Temperatures: Utilization of Boron Sulfides, *J. Am. Chem. Soc.*, 2004, **126**, 4676–4681.
13 A. A. Berseneva, V. V. Klepov, K. Pal, K. Seeley, D. Koury, J. Schaeperkoetter, J. T. Wright, S. T. Misture, M. G. Kanatzidis, C. Wolverton, A. V. Gelis and H.-C. zur Loye, Transuranium Sulfide via the Boron Chalcogen Mixture Method and Reversible Water Uptake in the $NaCuTS_3$ Family, *J. Am. Chem. Soc.*, 2022, **144**, 13773–13786.
14 H.-Y. Chen and P. W. Gilles, High Molecular Weight Boron Sulfides. V. Vaporization Behavior of the Boron-Sulfur System, *J. Am. Chem. Soc.*, 1970, **92**, 2309–2312.
15 H. Liu, H. Gong, K. Liu, K. Ding, J. Chen, Z. Liu and F. Rao, Electronic Excitation-Induced Semiconductor-Metal Transitions Enabling Ovonic Threshold Switching in Boron Telluride Glasses, *Chem. Mater.*, 2023, **35**, 6396–6404.
16 E. R. Franke and H. Schäfer, Zur Strukturchemie ternaerer Telluride der Alkali- und Erdalkalimetalle mit den Elementen der dritten Hauptgruppe, *Z. Naturforsch., B*, 1972, **27**, 1308–1315.
17 O. M. Aliev, Some General Features of Reactions between Chalcogenides of Elements of Subgroups IIIa and IIIb, *Inorg. Mater.*, 1980, **16**, 1027–1031.
18 *Bruker APEX4 Version 2009.5-1 Data Collection and Processing Software*, Bruker Analytical X-Ray Instruments, Inc., Madison, WI, 2009.
19 G. M. Sheldrick, *SADABS*, Bruker AXS, Inc., Madison, Wisconsin, USA, 2008.
20 G. M. Sheldrick, *XPREP Version 2008/2*, Bruker AXS Inc., Madison, 2018.
21 G. M. Sheldrick, SHELXT – Integrated Space-Group and Crystal-Structure Determination, *Acta Crystallogr., Sect. A: Found. Adv.*, 2015, **71**, 3–8.
22 G. M. Sheldrick, Crystal Structure Refinement with SHELXL, *Acta Crystallogr., Sect. C:Struct. Chem.*, 2015, **71**, 3–8.
23 A. L. Spek, Single-Crystal Structure Validation with the Program PLATON, *J. Appl. Crystallogr.*, 2003, **36**, 7–13.
24 P. Makuła, M. Pacia and W. Macyk, How To Correctly Determine the Band Gap Energy of Modified Semiconductor Photocatalysts Based on UV–Vis Spectra, *J. Phys. Chem. Lett.*, 2018, **9**, 6814–6817.
25 G. Kresse, Efficient Iterative Schemes for *Ab Initio* Total-Energy Calculations Using a Plane-Wave Basis Set, *Phys. Rev. B:Condens. Matter Mater. Phys.*, 1996, **54**(16), 11169–11186.
26 G. Kresse and J. Furthmüller, Efficiency of *Ab initio* Total Energy Calculations for Metals and Semiconductors Using a Plane-Wave Basis Set, *Comput. Mater. Sci.*, 1996, **6**(1), 15–50.
27 J. P. Perdew, Generalized Gradient Approximation Made Simple, *Phys. Rev. Lett.*, 1996, **77**, 3865–3868.
28 S. Jana, E. A. Gabilondo, M. Mongkhonratanachai, P. S. Halasyamani and P. A. Maggard, Eu(II)-Based Quaternary Chalcogenides with Noncentrosymmetric Structures Stabilized by Site Disorder of d^{10} Metal Cations, *Z. Anorg. Allg. Chem.*, 2025, **651**, e202500041.
29 Y. Hinuma, G. Pizzi, Y. Kumagai, F. Oba and I. Tanaka, Band Structure Diagram Paths Based on Crystallography, *Comput. Mater. Sci.*, 2017, **128**, 140–184.
30 A. M. Ganose, A. J. Jackson and D. O. Scanlon, SUMO: Command-Line Tools for Plotting and Analysis of Periodic Ab Initio Calculations, *J. Open Source Softw.*, 2018, **3**, 717.
31 M. Sun, X. Zhang, X. W. Xing, Z. Li, W. Liu, Z. Lin, W. Yin and J. Yao, Synthesis and Characterizations of Two Tellurides β-$BaGa_2Te_4$ and $Ba_5Ga_2Ge_3Te_{12}$ with Flexible Chain Structure, *Inorg. Chem.*, 2021, **60**, 14793–14802.
32 E. R. Franke and H. Schäfer, Zur Strukturchemie Ternärer Telluride Der Alkali- Und Erdalkalimetalle Mit Den Elementen Der 3. Hauptgruppe/On the Structural Chemistry of Ternary Tellurides of Alkali- and Earthalkalimetalls with the Group- (III) -Elements, *Z. Naturforsch., B*, 1972, **27**, 1308–1315.
33 H. Li, C. D. Malliakas, J. A. Peters, Z. Liu, J. Im, H. Jin, C. D. Morris, L.-D. Zhao, B. W. Wessels, A. J. Freeman and M. G. Kanatzidis, $CsCdInQ_3$ (Q = Se, Te): New Photoconductive Compounds As Potential Materials for Hard Radiation Detection, *Chem. Mater.*, 2013, **25**, 2089–2099.
34 Y. Luo, J. Yang, Q. Jiang, W. Li, D. Zhang, Z. Zhou, Y. Cheng, Y. Ren and X. He, Progressive Regulation of Electrical and Thermal Transport Properties to High-Performance $CuInTe_2$ Thermoelectric Materials, *Adv. Energy Mater.*, 2016, **6**, 1600007.
35 M.-Y. Lee, D. I. Bilc, E. Symeou, Y.-C. Lin, I.-C. Liang, T. Kyratsi and K.-F. Hsu, Synthesis, Crystal Structure and Thermoelectric Properties of a New Metal Telluride $Ba_3Ag_3InTe_6$, *Inorg. Chem. Front.*, 2017, **4**, 1458–1464.
36 R. Patschke, P. Brazis, C. R. Kannewurf and M. G. Kanatzidis, $Cu_{0.66}EuTe_2$, KCu_2EuTe_4 and $Na_{0.2}Ag_{2.8}EuTe_4$: Compounds with Modulated Square Te Nets, *J. Mater. Chem.*, 1999, **9**, 2293–2296.
37 X. Zheng, M. Boubeche, W. Wang, Z. Fang, J. Xin, J. Yang, Y. Xia, L. Zhang, W. Wu and D. Wu, Synthesis and

Characterization of Eu_2InTe_5: A New Layered Multitelluride and Its Thermoelectric Properties, *Phys. Status Solidi RRL*, 2022, **16**, 2200166.

38 I. Chung and M. G. Kanatzidis, Metal Chalcogenides: A Rich Source of Nonlinear Optical Materials, *Chem. Mater.*, 2013, **26**, 849–869.

39 J. P. Perdew, Density Functional Theory and the Band Gap Problem, *Int. J. Quantum Chem.*, 1985, **28**, 497–523.

40 S. Maintz, V. L. Deringer, A. L. Tchougréeff and R. Dronskowski, LOBSTER: A Tool to Extract Chemical Bonding from Plane-Wave Based DFT, *J. Comput. Chem.*, 2016, **37**, 1030–1035.

41 R. Nelson, C. Ertural, J. George, V. L. Deringer, G. Hautier and R. Dronskowski, LOBSTER: Local Orbital Projections, Atomic Charges, and Chemical-Bonding Analysis from Projector-Augmented-Wave-Based Density-Functional Theory, *J. Comput. Chem.*, 2020, **41**, 1931–1940.

42 (*a*) CCDC 2415584: Experimental Crystal Structure Determination, 2026, DOI: 10.25505/fiz.icsd.cc2m2m2f; (*b*) CCDC 2415585: Experimental Crystal Structure Determination, 2026, DOI: 10.25505/fiz.icsd.cc2m2m3g; (*c*) CCDC 2486668: Experimental Crystal Structure Determination, 2026, DOI: 10.25505/fiz.icsd.cc2pgl3w.